How Well Do Atmospheric General Circulation Models Capture the Leading Modes of the Interannual Variability of the Asian–Australian Monsoon?

Tianjun Zhou

LASG, Institute of Atmospheric Physics, Chinese Academy of Sciences, Beijing, China

Bo Wu

LASG, Institute of Atmospheric Physics, Chinese Academy of Sciences, and Graduate University of Chinese Academy of Sciences, Beijing, China

Bin Wang

Department of Meteorology, and International Pacific Research Center, University of Hawaii at Manoa, Honolulu, Hawaii

(Manuscript received 17 September 2007, in final form 25 August 2008)

ABSTRACT

The authors evaluate the performances of 11 AGCMs that participated in the Atmospheric Model Intercomparison Project II (AMIP II) and that were run in an AGCM-alone way forced by historical sea surface temperature covering the period 1979–99 and their multimodel ensemble (MME) simulation of the interannual variability of the Asian–Australian monsoon (AAM). The authors explore to what extent these models can reproduce two observed major modes of AAM rainfall for the period 1979–99, which account for about 38% of the total interannual variances. It is shown that the MME SST-forced simulation of the seasonal rainfall anomalies reproduces the first two leading modes of variability with a skill that is comparable to the NCEP/Department of Energy Global Reanalysis 2 (NCEP-2) in terms of the spatial patterns and the corresponding temporal variations as well as their relationships with ENSO evolution. Both the biennial tendency and low-frequency components of the two leading modes are captured reasonably in MME. The skill of AMIP simulation is seasonally dependent. December–February (DJF) [July–August (JJA)] has the highest (lowest) skill. Over the extratropical western North Pacific and South China Sea, where ocean–atmosphere coupling may be critical for modeling the monsoon rainfall, the MME fails to demonstrate any skill in JJA, while the reanalysis has higher skills. The MME has deficiencies in simulating the seasonal phase of two anticyclones associated with the first mode, which are not in phase with ENSO forcing in observations but strictly match that of Niño-3.4 SST in MME. While the success of MME in capturing essential features of the first mode suggests the dominance of remote El Niño forcing in producing the predictable portion of AAM rainfall variability, the deficiency in capturing the seasonal phase implies the importance of local air–sea coupling effects. The first mode generally concurs with the turnabout of El Niño; meanwhile, the second mode is driven by La Niña at decaying stage. Multimodel intercomparison shows that there are good relationships between the simulated climatology and anomaly in terms of the degree of accuracy.

1. Introduction

The thermal contrast between the Eurasian continent and the Indo-Pacific Ocean produces the powerful Asian–Australian monsoon (AAM) system. The AAM region, spanning from about 40° to 160°E and from 30°S to 40°N, covers one-third of the global tropics and subtropics (Wang 2006). The economy and society across the region are critically influenced by the evolution and variability of the monsoon. The AAM climate exhibits variability in a variety of time scales (e.g., Webster and Yang 1992; Hu 1997; Lau and Nath 2000; Wang 2001; Meehl and Arblaster 2002; Hu et al. 2003; Yu et al. 2004; Zhou and Yu 2005, 2006; Yang and Lau 2006; Yu and Zhou 2007; Zhou et al. 2008b). A better prediction of the monsoon variation may greatly benefit this populated region.

Corresponding author address: Dr. Tianjun Zhou, LASG, Institute of Atmospheric Physics, Chinese Academy of Sciences, Beijing 100029, China.
E-mail: zhoutj@lasg.iap.ac.cn

Unfortunately, numerical simulation of the AAM interannual variability has been a challenge. For example, the atmospheric general circulation models (AGCMs) that participated in the Atmospheric Model Intercomparison Project (AMIP) show little predictability in the all-Indian rainfall (Sperber and Palmer 1996). Kang et al. (2002a) assessed the performance of 10 AGCMs in simulating the climatological variations of summer monsoon rainfall over the Asian–western Pacific region. The model composite shows a reasonable performance in reproducing the climatological intraseasonal oscillation of precipitation. However, an examination on the tropical rainfall anomalies associated with the 1997/98 El Niño shows that most of the AGCMs have difficulty in simulating the negative rainfall anomalies over the Maritime Continent (Kang et al. 2002b). An assessment on the ensemble simulations of AAM anomalies in 11 AGCMs during the unprecedented El Niño period, September 1996–August 1998, shows that the simulated anomalous Asian summer rainfall has a pattern correlation considerably poorer than its counterpart in the tropical central and eastern Pacific (Wang et al. 2004). The long-term change of AAM rainfall is also difficult to simulate with observational sea surface temperature (SST) forcing (Zhou et al. 2008a).

The difficulty in simulating and predicting AAM rainfall is partially related to the strategies of the AGCM-alone simulation. Recent studies suggested that local monsoon–warm pool ocean interactions should be considered in the prediction of summer monsoon rainfall (Wang et al. 2003, 2004; Wu and Kirtman 2005; Kumar et al. 2005). The poor performance in simulation of Asian summer monsoon variability with AGCMs forced by observed SST is attributed to the experimental design, in which the atmosphere is forced to respond to the specified SSTs, while in nature the SSTs are also partly forced by the atmosphere (Wang et al. 2004). In the absence of the monsoon–ocean interaction, the SST–rainfall correlations yielded by AGCMs are at odds with observations in some portions of the AAM domain (Wang et al. 2005).

Previous studies on the AAM predictability focused on the total rainfall. Because of the chaotic internal dynamics of the atmospheric motion, it is unrealistic to demand the predictability of the whole climate evolution. Determining the predictability of AAM and identifying the sources of predictability are of central importance in seasonal prediction. A recent observational analysis has identified two statistically distinguished modes of the AAM: The first mode exhibits a prominent biennial tendency and concurs with the turnabout of warming to cooling in the equatorial eastern-central Pacific, and the second mode leads the Pacific warming by 1 yr, pro-

viding a precursor for El Niño/La Niña development (Wang et al. 2008a,b). It provides a new perspective of the seasonal spatiotemporal structure for tropical biennial oscillation (Meehl and Arblaster 2002). The two major modes provide useful metrics for gauging the AAM system variability in climate models. Wang et al. (2008b) evaluated the performances of 10 state-of-the-art coupled climate models in predicting the observed two major modes of AAM rainfall and found a reasonable 1-month lead prediction.

The leading modes of the interannual variations of AAM are likely more predictable than other higher modes. While available analyses suggested that ocean–atmosphere coupled models have excellent performances in reproducing these leading modes (Wang et al. 2008b), how well the AGCM-alone models reproduce these leading modes remains an open question. Previous analyses on the AGCM-alone experiments focused on the total rainfall rather than the leading modes. Some evidences suggest that both local and remote SST forcing contribute to the generation of major circulation anomalies associated with these leading modes (Li et al. 2005, 2006). Therefore, it is important to assess how well the AMIP-type AGCM simulation captures the leading modes of the interannual variability of AAM. This is the major purpose of present study. We analyze the outputs of 11 AMIP II models to obtain insights into this issue.

The rest part of the paper is organized as follows. Section 2 describes the methodology and datasets. Section 3 examines whether the major modes of the interannual variability of AAM can be captured by AMIP simulation. Section 4 discusses the difference of AMIP simulation with reanalyses and fully coupled models. The driving mechanisms of SST forcing to the AAM leading modes are also discussed. Section 5 summarizes the study.

2. The data and analysis procedure

a. The models and data

The data used in this study were derived from the World Climate Research Programme's (WCRP's) Coupled Model Intercomparison Project phase 3 (CMIP3) multimodel dataset. The results of 11 AGCMs that were driven by monthly historical SST and sea ice are examined. Table 1 shows a brief summary of these models. Different horizontal/vertical resolutions were used in these models. Documentations of the models are referred to the Web site of the U.S. Department of Energy's Program for Climate Model Diagnosis and Intercomparison (PCMDI; see http://www-pcmdi.llnl.gov/ipcc/about_ipcc.php). In the

TABLE 1. Description of 11 atmospheric general circulation models.

Institute	AGCM	Resolution	Name used in the discussion
Met Office (UKMO)	HadGAM1	N96L38	HadGEM1
NCAR	CAM3	T85L26	CCSM3
MRI	—	T42L30	CGCM2.3.2a
MPI	ECHAM5	T63 L32	ECHAM5
Center for Climate System Research (CCSR)	MIROC3.2(medres)	T42L20	MIROC3.2(medres)
CCSR	MIROC3.2(hires)	T106 L56	MIROC3.2(hires)
INM	—	4.0° lat × 5.0° lon L21	INM-CM3.0
Institute of Atmospheric Physics (IAP)	GAMIL	2.8° lat × 2.8° lon L26	FGOALS-g1.0
National Aeronautics and Space Administration (NASA) GISS	—	4.0° lat × 5.0° lon L20	GISS-ER
GFDL	—	2.0° lat × 2.5° lon L24	GFDL AM2
CNRM	—	T42 L45	CNRM-CM3

present study, we focus on evaluating the model outputs covering the period 1979–99. Note in WCRP's CMIP3 multimodel dataset bank, the outputs of AMIP II experiments are labeled with the names of corresponding ocean–atmosphere coupled models. Some AGCMs do not have specific names. For brevity, we use the names of coupled models to represent the AGCM components in the following discussion.

The verification datasets include 1) the Climate Prediction Center Merged Analysis of Precipitation (CMAP) data (Xie and Arkin 1997); 2) the National Centers for Environmental Prediction–National Center for Atmospheric Research (NCEP–NCAR) Reanalysis (hereafter, NCEP) data (Kalnay et al. 1996); 3) the NCEP/Department of Energy (DOE) AMIP II Reanalysis (hereafter, NCEP-2) data (Kanamitsu et al. 2002); and 4) the 40-yr European Centre for Medium-Range Weather Forecasts (ECMWF) Re-Analysis (hereafter, ERA-40) data (Uppala et al. 2005). The observational 850-hPa wind fields were obtained from NCEP, NCEP-2, and ERA-40. 5) The observational SST data are from the Global Sea Ice and Sea Surface Temperature (GISST) dataset (Rayner et al. 2003).

b. Analysis procedure

To depict the interannual variability of AAM system, we apply the season-reliant EOF (S-EOF) analysis method (Wang and An 2005). The S-EOF is capable of depicting seasonally evolving anomalies throughout a full calendar year. We adopt the concept of "monsoon year" (Meehl 1987; Yasunari 1991), which spans from the summer of year 0, referred to as July–August (JJA)(0), to the spring of the following year (year 1), called March–May (MAM)(1). A covariance matrix is constructed using four consecutive seasonal mean anomalies for each year; that is, the anomalies for JJA(0), September–November (SON)(0), December (0)–February (1) [D(0)JF(1)], and

MAM(1) are treated as a "yearly block," labeled year 0. After the EOF decomposition is performed, the yearly block is then divided into four consecutive seasonal anomalies. Therefore, we obtain a seasonal pattern of monsoon anomalies in each monsoon year for each eigenvector.

Our analysis focuses on rainfall. We apply the S-EOF analysis to both observed and simulated seasonal mean rainfall anomalies, which are the departures from the mean annual cycle derived from the period 1979–99. Before performing S-EOF analysis, the data are linearly detrended. We consider the AAM region extending from 40°E to 160°E, and 30°S to 40°N. We mainly present the results of multimodel ensemble (MME).

3. The major modes of AAM variability in MME AMIP simulation

a. The leading modes and the associated principal components in MME

The observed leading modes of the AAM system are revealed by applying the S-EOF analysis to CMAP rainfall seasonal anomalies (1979–99). The seasonal evolutions of the spatial patterns of AAM rainfall anomalies associated with S-EOF1 are shown in Fig. 1a. Also shown are the NCEP-2 850-hPa wind anomalies (vectors), which are linearly regressed against the first principal component (PC1). The spatial patterns of leading modes resemble that of Wang et al. (2008b), which used a different data length of 1981–2002. These two leading modes serve as observational metrics in our following model evaluations. To facilitate model comparison, we describe the main features of the dominant modes here. The notable feature of S-EOF1 (Fig. 1a) is two seasonal anticyclonic anomalies, the south Indian Ocean (SIO) and the western North Pacific (WNP)
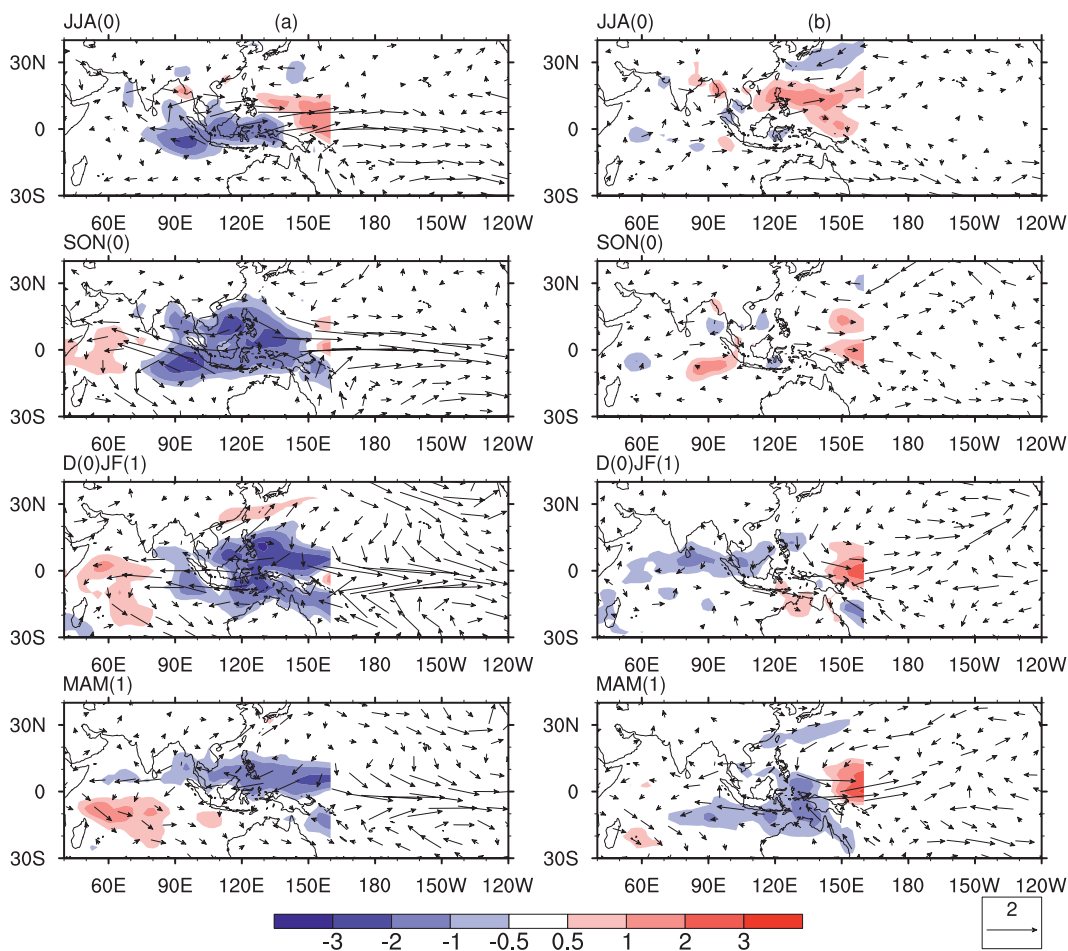
FIG. 1. Spatial patterns of the first S-EOF mode of seasonal precipitation anomalies from JJA(0) to MAM(1) (color shading; mm day^{-1}) and the NCEP-2 850-hPa wind anomalies (vectors; m s^{-1}), which were linearly regressed against the corresponding principal component. (b) Same as in (a) except for the second S-EOF mode.

anticyclones (AC). During JJA(0), an anomalous AC ridge extends from the Maritime Continent to the southern tip of India with enhanced monsoon westerly extends from India to the western Pacific. During SON(0), the SIO AC anomalies and the zonal wind divergence around the Maritime Continent are established. From SON(0) to D(0)JF(1), the SIO AC slightly weakens, meanwhile a new AC forms over the Philippine Sea. From D(0)JF(1) to next MAM(1), the SIO and WNP ACs remain but weaken.

Associated with the anomalous circulation patterns, the dry and wet centers exhibit prominent seasonal evolutions (Fig. 1a). During JJA(0), there are less rainfall over the Maritime Continent and equatorial eastern Indian Ocean. An enhanced rainfall is evident over the equatorial western Pacific and the Philippine Sea. During SON(0), the dry anomalies over the Maritime Continent intensify and expand northward and eastward, which covers the Philippine archipelago and the

entire tropical South Asia; meanwhile, the western Indian Ocean becomes wetter than normal and a dipole rainfall pattern develops in the tropical Indian Ocean. During D(0)JF(1), the center of dry anomalies shifts to the Philippine Sea. During MAM(1), the dry anomalies decay rapidly and move further eastward with dry center locating in the equatorial western Pacific. Rainfall increases in the tropical western Indian Ocean.

The spatial patterns of S-EOF2 in observation are shown in Fig. 1b. A large-scale cyclonic anomaly forms over the WNP in the summer to fall, followed by a continuous southeastward movement and strengthening through the following winter and next spring. Following the seasonal evolution of the WNP cyclonic wind anomalies, excessive rainfall occurs over the WNP in JJA(0), and then shifts equatorward in SON(0). Dry anomalies develop in the northern Indian Ocean and South China Sea in D(0)JF(1), and over the eastern Indonesia and northern Australia in MAM(1).

The time series of the PCs of the first and second S-EOF modes of seasonal rainfall anomalies obtained from CMAP data and AMIP simulation are shown in Figs. 2a,b. The lead–lag correlation coefficients between the two PCs and the Niño-3.4 SST anomalies are presented in Figs. 2c,d. The observed first mode shows a maximum positive correlation coefficient that exceeds 0.9 with a Niño-3.4 SST anomaly (SSTA) in D(0)JF(1), indicating that the first S-EOF mode concurs with El Niño turnaround. The second mode shows a maximum correlation coefficient (about 0.65) leading El Niño by about one year, and a minimum negative correlation coefficient (about −0.55) lagging the Niño-3.4 index by about one year, signaling the transition from La Niña to El Niño (Fig. 2d).

The seasonal evolution of S-EOF1 in MME well resembles the observation (Fig. 3a). For the rainfall anomalies associated with S-EOF1, the anomalous patterns from JJA(0) to MAM(1) are well simulated, with a pattern correlation larger than 0.65. Larger correlation coefficients (0.75–0.81) are found during SON(0) and D(0)JF(1), suggesting that, during the developing phase of ENSO, the models have acceptable performances in capturing the rainfall anomalies over the Maritime Continent and western Pacific. During the decaying phase of ENSO, that is, MAM(1), the resemblance of MME with the observation decays rapidly, indicating the weakening tendency of SST forcing in causing rainfall anomalies over the Maritime Continent.

The seasonal evolutions of SIO and WNP ACs are also reasonably captured in MME. The well simulated features include the anomalous AC ridge extending from Maritime Continent to the southern tip of India in JJA(0), the zonal wind divergence around the Maritime Continent during SON(0), the WNP AC over the Philippine Sea during D(0)JF(1) and its persistence up to MAM(1).

A deficiency of MME lies in the SIO AC. The simulated SIO AC during SON(0) is weaker than that in reanalysis. From SON to DJF, the SIO AC slightly strengthens and responds with delay to ocean forcing, which is contrary to the observation. The reason for this deficiency will be elaborated in the following discussion section.

The pattern of S-EOF2 in MME is shown in Fig. 3b. The seasonal evolution of WNP cyclonic anomalies is well captured. Following the evolution of anomalous circulation, the rainfall anomalies from SON(0) to MAM(1) are simulated reasonably, with map correlation coefficients ranging from 0.56 to 0.81 (Fig. 3b). However, the JJA(0) pattern is poorly simulated, having a pattern correlation of 0.41. The reason is largely due to the lack of significant SSTA forcing in the transitional phase of ENSO. In the following fall to spring,
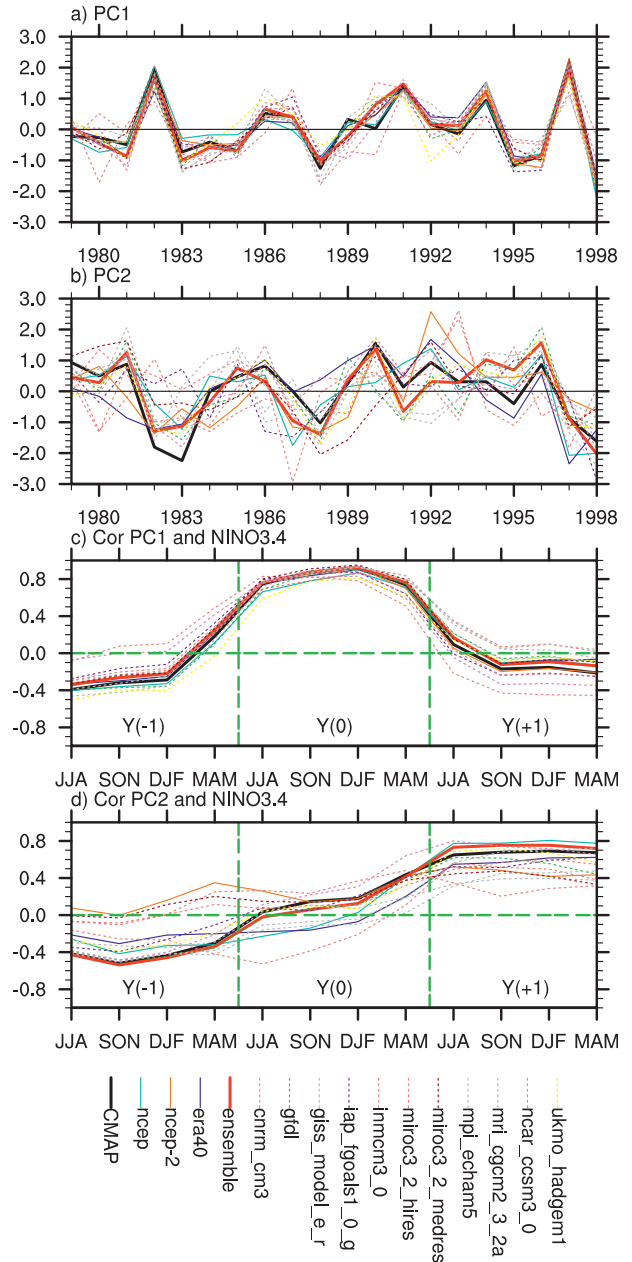

FIG. 2. Principal components of (a) the first and (b) the second S-EOF modes of seasonal precipitation anomaly obtained from CMAP observation (black thick solid), MME (red thick solid), reanalysis datasets (colored thin solid lines), and each model simulation (thin dotted coloring). (c) Lead–lag correlation coefficients between the first S-EOF principal component and the Niño-3.4 SST index. (d) The same as in (c) except for the second S-EOF principal component. Observation (black thick solid), MME (red thick solid), reanalysis datasets (colored thin solid lines), and each model (thin dotted coloring).
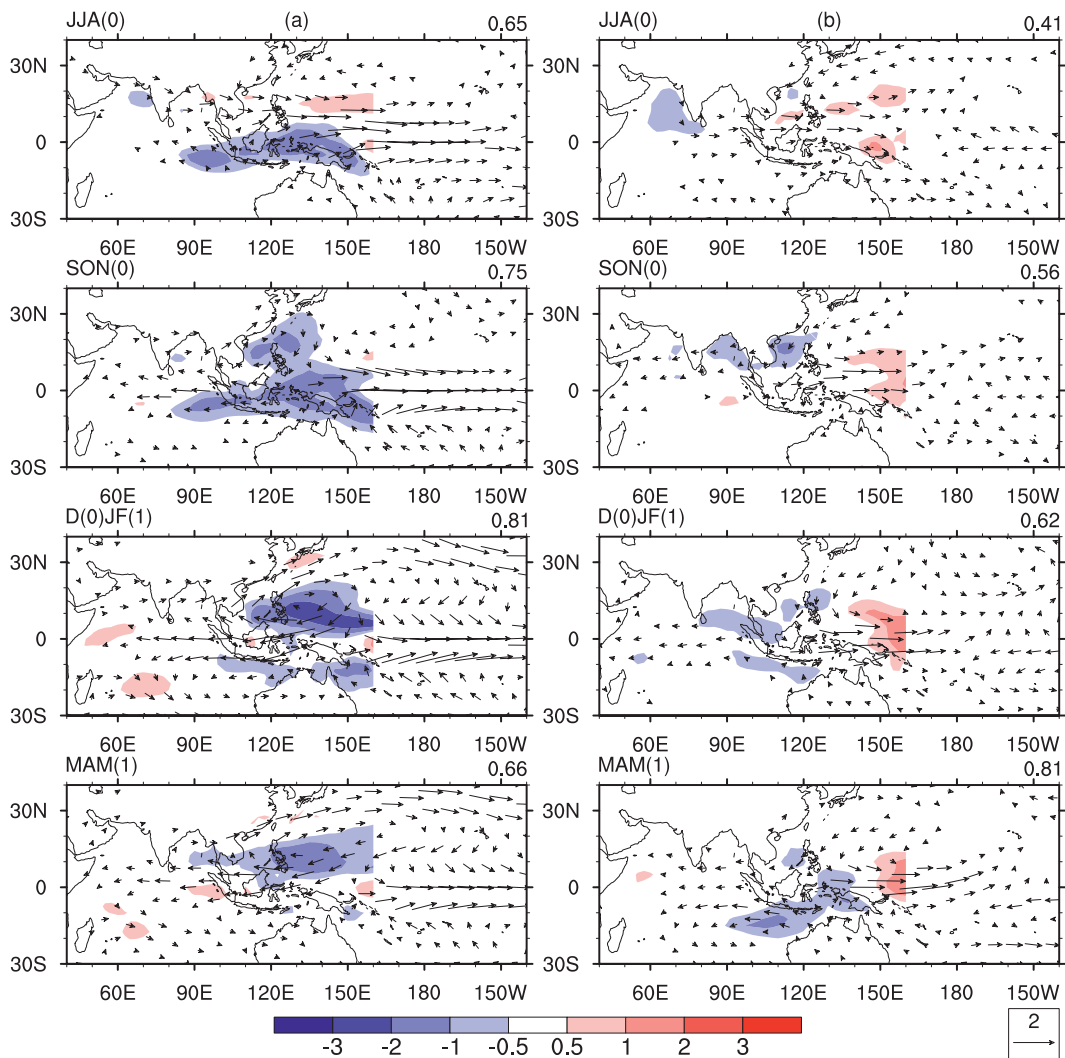
FIG. 3. Same as Fig. 1 but for AMIP MME. Spatial pattern correlations of rainfall anomalies with the observation are marked at the upper-right corner of each panel.

that is, SON(0), D(0)JF(1) and MAM(1), the anomaly patterns of S-EOF2 are simulated well. Nevertheless, while the MME reasonably captures the observed rainfall anomaly patterns, its amplitudes of rainfall anomalies are generally weaker than the observations. This is expected, since working with ensembles increases the correlation but decreases the amplitude (Li 1999; Zhou and Yu 2004).

The temporal variations of the leading modes are also well simulated in MME (Fig. 2a). The correlation coefficient between the observed and simulated PC time series is 0.95 (0.85) for S-EOF1 (S-EOF2; Figs. 2a,b). Furthermore, Fig. 2c indicates that the MME reasonably captures the observed overall relationship between ENSO and AAM. In addition, as shown in Fig. 2b, the spread among the models in PC2 is larger than that in

PC1, suggesting the first mode has a higher reproducibility than the second mode.

In summary, the MME reproduces faithfully the major features of two observed leading modes of the interannual variability of AAM seasonal rainfall, suggesting in case the SST anomalies are predictable, the dominant modes of the interannual variability of AAM are highly reproducible.

b. Multimodel intercomparisons

To show the differences of AMIP models in simulating the leading modes of the interannual variability of AAM, it is useful to evaluate the performance of each individual model. The results of three reanalysis datasets, namely, the ERA-40, NCEP, and NCEP-2, are also
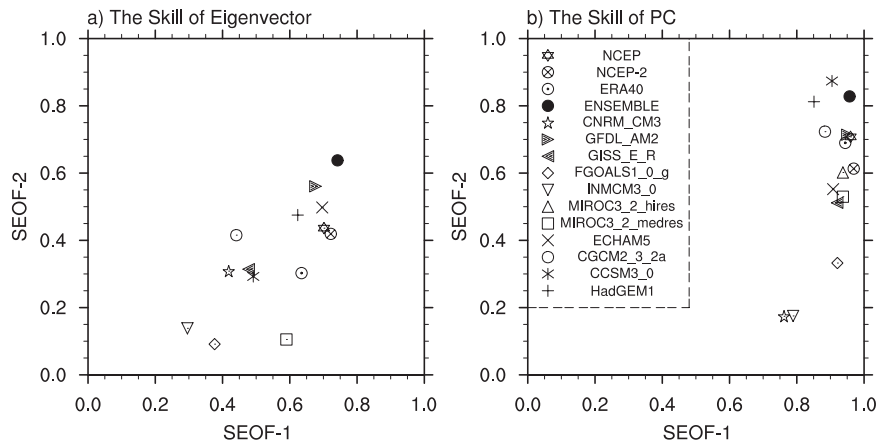
FIG. 4. Comparison of the performances of the AMIP MME, individual simulations, and three (NCEP, NCEP-2, and ERA-40) reanalysis datasets against the observed (CMAP) two dominant S-EOF modes of seasonal mean precipitation anomalies. The abscissa and ordinate represent, respectively, correlation coefficients between the observed and simulated (reanalyzed) anomalies for the first and second modes. (a) The spatial correlation skill of eigenvector and (b) the temporal correlation skill of principal component.

compared. We use correlation coefficients to assess the skills of both the spatial patterns (Fig. 4a) and PCs (Fig. 4b) for the two major modes. In Fig. 4, the CMAP is used as the ground "truth" for comparison. The MME is better than each individual model. Among the 11 AGCMs, the leading modes derived from ECHAM5 and Hadley Centre Global Environmental Model version 1 (HadGEM1) models are generally better than those derived from other models. Six models, namely, the Meteorological Research Institute (MRI) Coupled General Circulation Model version 2.3.2a (CGCM2.3.2a), the Centre National de Recherches Météorologiques Coupled Global Climate Model version 3 (CNRM-CM3), the Goddard Institute for Space Studies Model E-R (GISS-ER), Community Climate System Model, version 3 (CCSM3), and the Model for Interdisciplinary Research on Climate 3.2, high-resolution and medium-resolution versions [MIROC3.2(hires) and MIROC3.2(medres)], show comparable performances, with map correlation coefficients ranging from 0.4 to 0.6. Two models, namely, the Institute of Numerical Mathematics Coupled Model, version 3.0 (INM-CM3.0) and Flexible Global Ocean–Atmosphere–Land System Model gridpoint version 1.0 (FGOALS-g1.0), have low map correlation coefficients ranging from 0.2 to 0.4. The performances of AGCMs in deriving the second mode are generally poorer than those in deriving the first mode. A number of models, namely INM-CM3.0, FGOALS-g1.0, and MIROC3.2(medres), have pattern correlation coefficients less than 0.2. Four models, namely, CCSM3, CNRM-CM3, GISS-ER, and CGCM2.3.2a, have map correlation coefficients ranging from 0.25 to 0.41.

In terms of temporal evolution (Fig. 4b), most models show considerably high temporal correlation coefficients for both two major modes. The correlation coefficients for S-EOF1 are generally higher than those for S-EOF2: The correlation coefficients for S-EOF1 range from 0.8 to 0.9, while those for S-EOF2 range from 0.55 to 0.85. Three models, namely, CNRM-CM3, INM-CM3.0, and FGOALS-g1.0, have temporal correlation coefficients less than 0.4.

The leading modes derived from the MME simulations are comparable to those derived from reanalysis datasets. This is seen in both the spatial patterns and the temporal evolutions. The leading modes derived from Geophysical Fluid Dynamics Laboratory Atmosphere Model version 2 (GFDL AM2), HadGEM1, and ECHAM5 simulations are comparable to, or even slightly better than, those derived from the reanalysis datasets. These three models also show considerably higher spatial and temporal correlation coefficients than any other model for both two major modes.

c. Fractional variance accounted for by the leading modes

The percentage variance accounted for by the first six eigenvalues of the S-EOF analysis of AAM rainfall is shown in Fig. 5. The unit standard deviation of the sampling errors associated with each percentage eigenvalue is also shown. The S-EOF1 (S-EOF2) accounts for 27.4% (10.6%) of the total variance. According to the rule of North et al. (1982), the observed first two leading modes are well distinguished from each other in terms of the sampling error bars, and hence are statistically
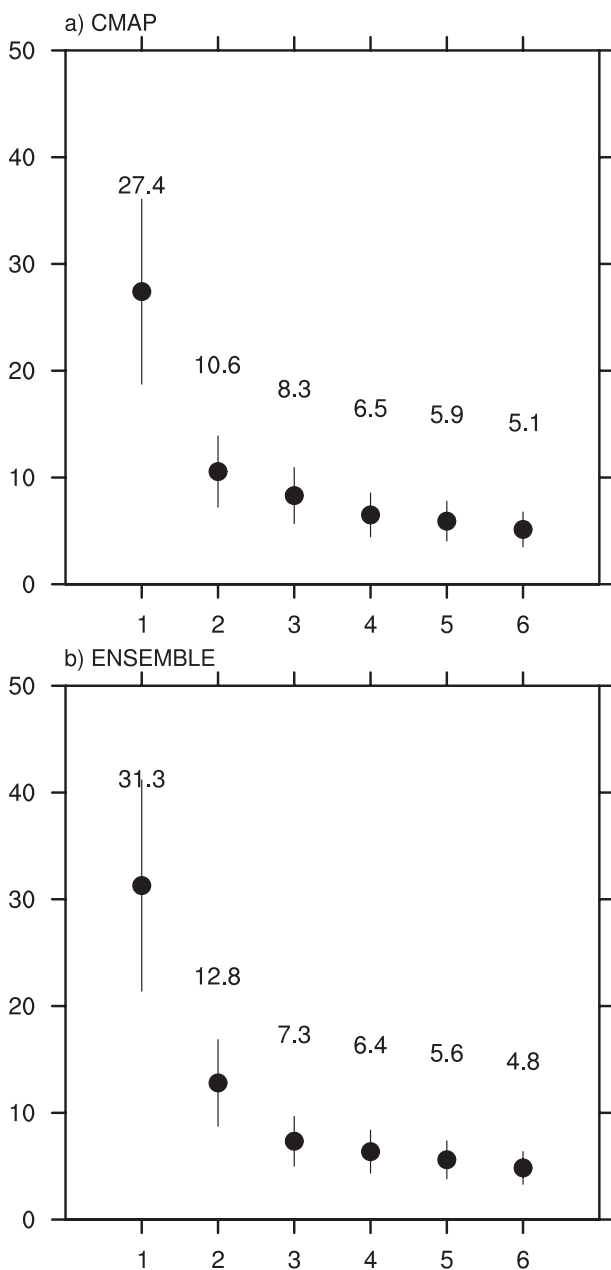
FIG. 5. Percentage variance (%) explained by the first six S-EOF modes of seasonal precipitation anomalies obtained from (a) CMAP and (b) MME simulation. The bars represent one std dev of the sampling errors.

TABLE 2. The percentage variances accounted for by the first two major modes in observation and simulations.

Data	S-EOF 1 (%)	S-EOF 2 (%)
CMAP	27.4	10.6
NCEP	23.8	9.7
NCEP-2	18.3	8.9
ERA-40	17.6	11.1
CNRM-CM3	21.6	11.0
GISS-ER	18.8	11.1
FGOALS-g1.0	18.9	11.9
INM-CM3.0	19.9	11.8
MIROC3.2(hires)	18.7	8.6
MIROC3.2(medres)	18.9	11.8
ECHAM5	22.0	15.1
CGCM2.3.2a	24.7	13.3
CCSM3	18.8	9.4
HadGEM1	15.9	10.8
GFDL AM2	19.0	12.0
Model ensemble	31.3	12.8

The fractional variance derived from MME is higher than any individual model.

The power spectrum density distributions and corresponding red noise of the first and second PC time series are shown in Fig. 6. In the observation, the first mode has a major spectral peak on 2.5 yr and a secondary peak around 4–6 yr. The MME captures both the quasi-biennial (2.5 yr) and low-frequency (4–6 yr) peaks reasonably. In the second mode, both the observation and MME show low-frequency spectral peaks around 5 yr, but the simulated variances are larger than the observation. The observed second mode also has a minor peak around 2.8 yr, which is partly captured by MME.

d. Seasonal dependence of the skill in AMIP simulation

The MME has a reasonable performance in capturing the leading modes of AAM rainfall variability. Since the statistics shown above are done for the total four consecutive seasons, in order to understand the mechanism it is useful to compare the skills during four seasons. We show the pattern correlation coefficients for four seasons in Fig. 7. For S-EOF1 of MME, the map correlation coefficients are 0.65 for JJA, 0.75 for SON, 0.81 for DJF, and 0.66 for MAM. The skill is the highest (lowest) in winter (summer). For S-EOF2 of MME, the map correlation coefficients are 0.41 for JJA, 0.56 for SON, 0.62 for DJF, and 0.81 for MAM. The result of spring is the best, while that of summer is still the worst. This validates Wang et al. (2004)'s argument that treating the atmosphere as a response to SST forcing may inherently be unable to correctly simulate the summer monsoon rainfall variations. The neglect of atmospheric feedback leads to the poor performance of AMIP simulation in reproducing

significant. The first two modes derived from MME have similar levels of statistical significance as the observed counterparts; namely, the S-EOF1 (S-EOF2) accounts for 30.3% (12.5%) of the total variance. Table 2 shows how the percentage variances accounted for by the first two major modes vary among different models, as well as observational dataset and reanalysis datasets.
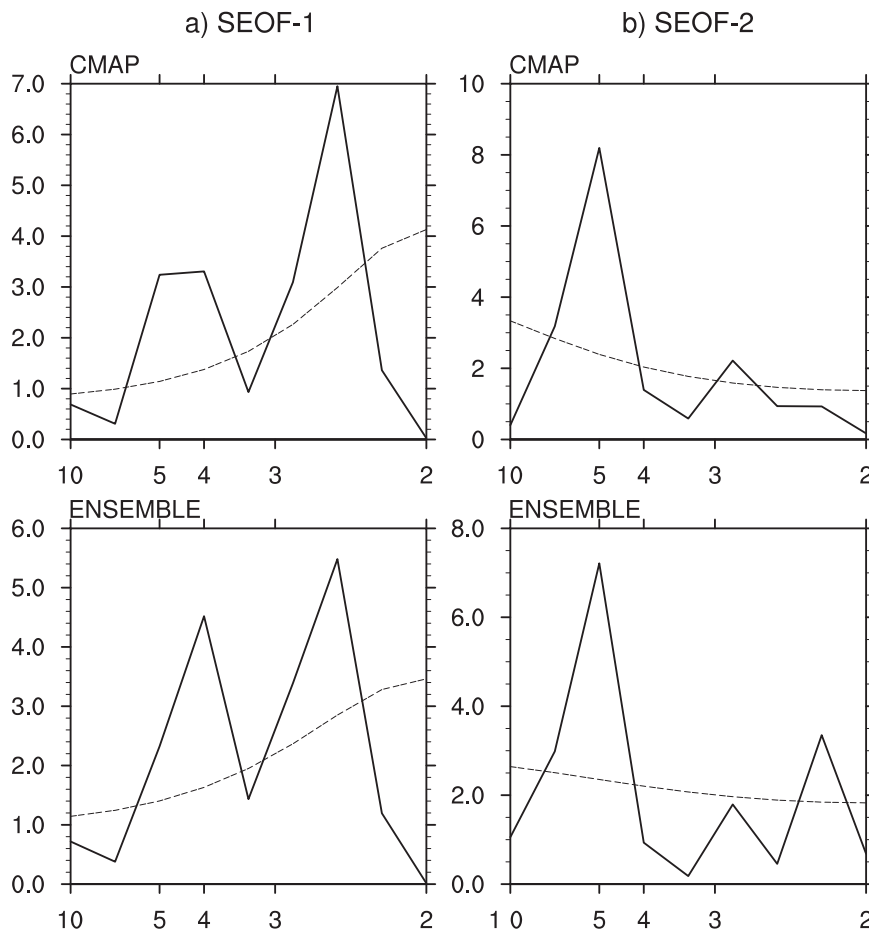
a) SEOF-1

b) SEOF-2

FIG. 6. The power spectrum density (solid line) and red noise (dashed line) of (a) the first and (b) the second S-EOF principal component of seasonal precipitation anomaly obtained from (top) CMAP observation and (bottom) MME simulation.

the dominant modes of summertime AAM rainfall variability. In addition, the relative better skills during winter (DJF) and transitional seasons (SON and MAM) indicate that the ocean-driving mechanism partly works during these seasons; namely, the atmospheric feedback to ocean is weak and it is more reasonable than JJA to treat the atmosphere as a response to ocean forcing.

A good spatial pattern correlation does not always indicate a good intensity. We further measure the intensities of simulated dominant modes by the root-mean-square (rms) of rainfall anomalies (figures not shown). The rms of MME is significantly lower than that of individual model, suggesting that the MME tends to underestimate the total variance while it successfully captures the observed spatial pattern and temporal evolution of the dominant modes. In addition, we have examined the relationship between the dominant modes and the accuracy of model climatology (figures not shown). The results indicate that an accurate climatol-

ogy usually coincides with a good anomaly pattern associated with the first mode during all seasons except for JJA. The skill of simulated second mode is proportional to the skill of corresponding climatology of individual model. The models with a larger (smaller) climatological mean rainfall than the observation generally simulate larger (smaller) rainfall anomalies than the observation. The MME has the highest degree of accuracy of both the climatology and the anomaly.

4. Discussion

a. The difference of AMIP simulations with fully coupled models

The above analyses show that the MME SST-forcing simulation could partly capture the first two leading modes of interannual rainfall variability over the AAM domain. How about the skills of AMIP models in simulating the total rainfall change? We show the correlation
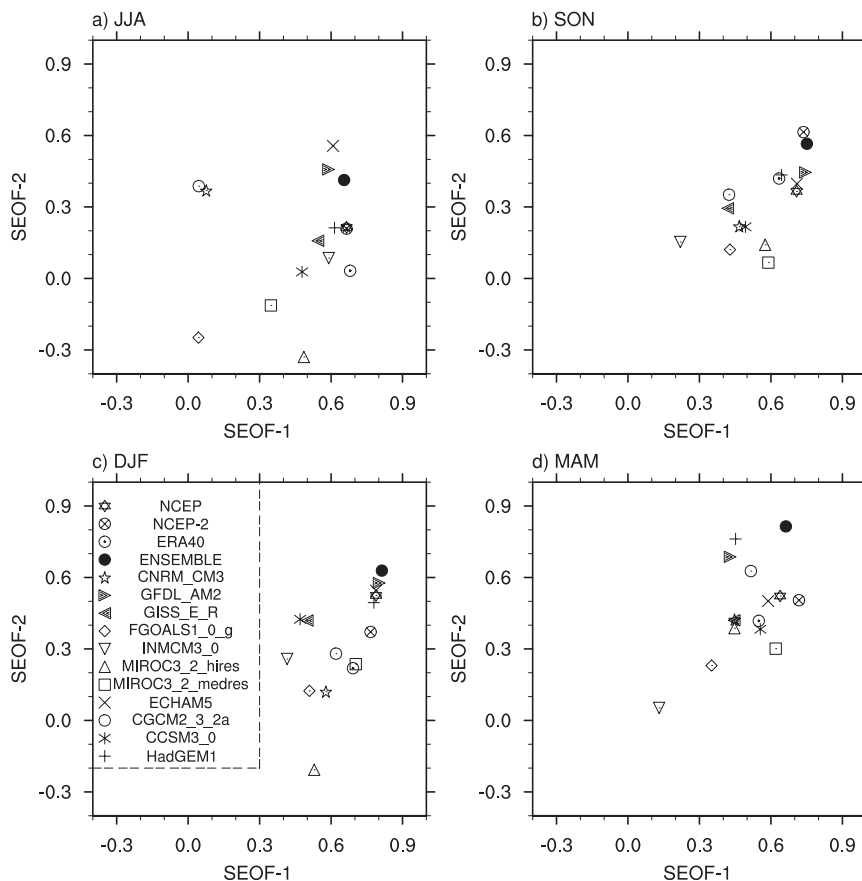
FIG. 7. Same as Fig. 4a but for four seasons: (a) JJA, (b) SON, (c) DJF, and (d) MAM.

of rainfall anomalies between the observation and the MME in Fig. 8. Although the first two leading modes account for 38% of the total variance, the fractional variance vary with location and season. We show percentage variance of rainfall anomalies accounted by the first leading mode in Fig. 8 as contours. The region having significant positive correlations coincides well with that having large fractional variance. During JJA, there are significant positive correlations over the Maritime Continent, equatorial eastern Indian Ocean, and subtropical western Pacific. The first major mode accounts for over 40% of the total variance over these regions. The skill over the WNP, the South China Sea, and the Bay of Bengal is low, which is consistent with Wang et al. (2005) and may be resulted from the neglect of air–sea feedback. From SON to DJF and next MAM, the seasonal variations of regions covered by significant positive correlations generally follow those of the regions having large fractional variance accounted by the first major mode. The consistency indicates that the first mode covers a large portion of the predictable part of total rainfall.

The above comparison shows that the resemblance of the simulated dominant modes with the observed one does not contradict with the previous claim that ocean–atmosphere coupling is critical for modeling the monsoon rainfall. The MME has deficiency in producing the intensity of rainfall anomalies, which may be partly due to the limitation of AMIP simulation in reproducing the seasonal phase of circulation patterns. The rainfall anomalies over the AAM domain are dominated by the seasonal varying SIO and WNP ACs. We compare the strength of tropical SIO and WNP ACs in MME with that in the reanalysis. We compute the anticyclonic vorticity anomalies for SIO in the region of 5°–20°S, 60°–100°E and for WNP in the region of 5°–20°N, 120°–160°E. In the reanalysis, the anomalous SIO AC begins in JJA(0), develops rapidly and reaches its peak in SON(0), and then decays over the next two seasons (Fig. 9a). The WNP AC begins in SON(0) and rapidly develops in D(0)JF(1), attains its peak in the following spring MAM(1), and then persists through the next summer (Fig. 9a). A comparison with the Niño-3.4 SST anomaly suggests the evolutions of SIO and WNP ACs
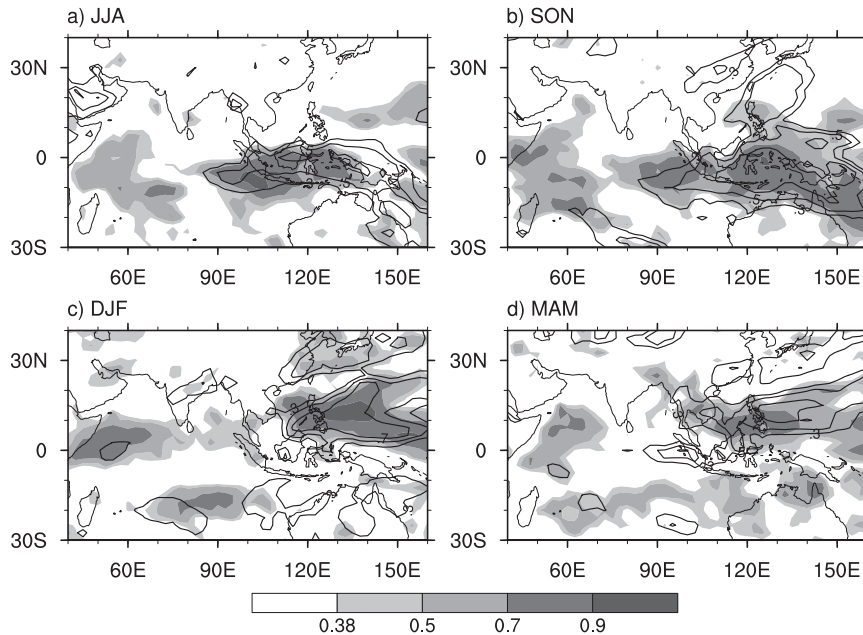
FIG. 8. The spatial pattern of correlation coefficients between the observed and AMIP MME simulated rainfall anomalies. Only correlations statistically significant at the 10% level are shaded. The percentage variance accounted by the first major mode is shown as contours, which start from 30% with an interval of 20%. (a) JJA, (b) SON, (c) DJF, and (d) MAM.

are not strictly in phase with ENSO forcing. Wang et al. (2000) showed that the western and eastern pacific SST anomalies contribute about equally to the WNP AC. The mechanism was discussed in detail by Wang and Zhang (2002). In AMIP simulation, however, the seasonal evolutions of both SIO and WNP ACs strictly match that of Niño-3.4 SST, implying that they are largely driven by remote ENSO forcing (Fig. 9b). In coupled models, the SIO (WNP) AC peaks in fall (next spring), which is not exactly in phase with ENSO forcing (Wang et al. 2008b). This difference reflects the effects of local air–sea coupling, which can modify the atmospheric response to remote oceanic forcing. The strengths of two ACs in MME are also different from those of the reanalysis that are associated with deficiencies in the simulated intensities of rainfall anomaly.

In addition, the skill of AMIP simulation in reproducing the first mode is seasonally dependent: DJF has a better pattern correlation with the observation than JJA, with 0.85 versus 0.61. This seasonal difference suggests that the local monsoon–warm pool ocean interaction should be more active (inactive) during JJA (DJF). This hypothesis is also supported by the significant positive correlations over the WNP during DJF shown in Fig. 8c. Wang et al. (2000) showed that given local western Pacific SST forcing the WNP AC can be partly reproduced during DJF. During transitional seasons such as SON and MAM, the impact of local air–sea

interaction on the first S-EOF mode should be less than that during JJA, as evidenced by the better pattern correlations between the observation and the simulation (see Fig. 7).

b. The difference of AMIP simulations with reanalysis data

Our analysis suggests that the MME has comparable skills with the reanalysis in capturing the observed leading modes of interannual variability of AAM. The reanalysis datasets include at least a part of the coupling effects, because the models are updated continuously every 6–12 h with observed wind, pressure, and temperature data, which themselves are the result of both the real SST forcing and the real atmosphere–ocean feedbacks. Therefore, the reanalysis results are at least partially driven by the real coupling and in a way may be considered as if they were produced from somewhat incomplete coupled models. If ocean–atmosphere coupling is critical for modeling the monsoon rainfall as claimed previously, the reanalysis results should have better skills than the AGCMs in simulating the interannual variability of the total rainfall. To verify this argument, the correlation pattern of rainfall anomalies between NCEP-2 and CMAP are shown in Fig. 10. In comparison with Fig. 8, the reanalysis shows comparable skills over the tropical regions, where are dominated by the major modes of interannual variability.
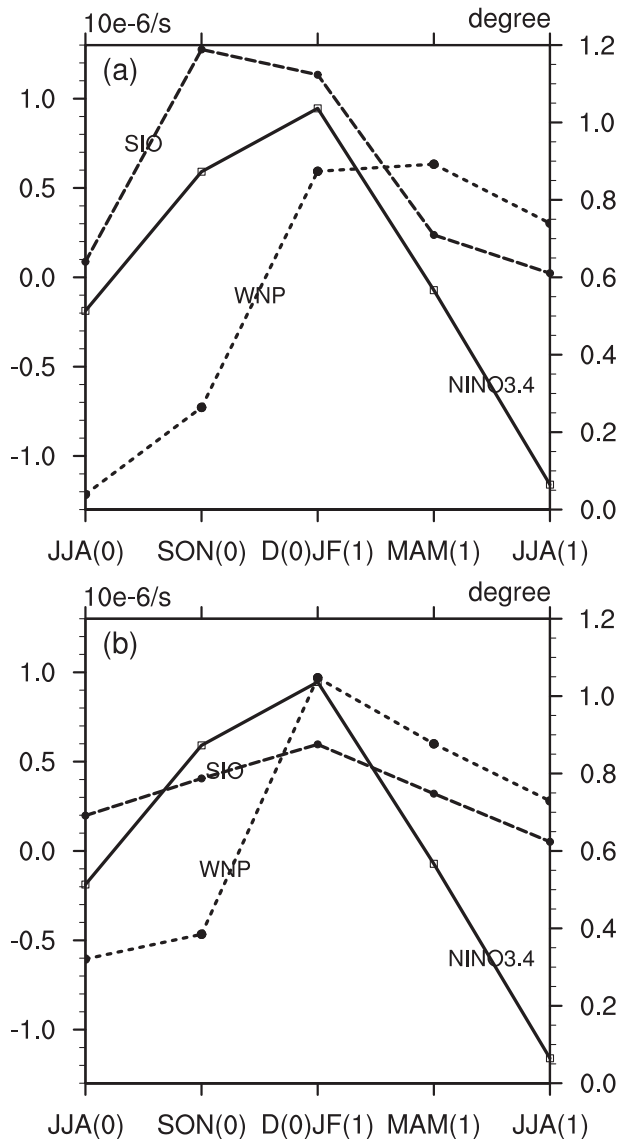
FIG. 9. Seasonal variations of the anomalous SIO anticyclonic vorticity averaged over the region of 5°–20°S, 60°–100°E, and the anomalous WNP anticyclonic vorticity averaged over the region of 5°–20°N, 120°–160°E. The sign of WNP vorticity is reversed for easy comparison. Shown also are the regressed Niño-3.4 SST anomalies with respect to the first principal component of the S-EOF mode. (a) NCEP-2; (b) AMIP MME.

Over the extratropical ocean and land areas, however, the reanalysis is far better than the MME. Significant positive correlations are evident in the WNP and South China Sea in JJA, where the MME barely demonstrates any skill. Since the reanalysis data contain information from both the one-way forced leading modes and the atmospheric feedback from the 6–12-h updating cycle, the better total skill over these regions means that the

gain due to the atmospheric feedback adequately compensates the deficit related to the one-way SST forcing.

c. The forcing mechanism of S-EOF2

Previous analysis suggested that the remote El Niño forcing, the monsoon–warm pool ocean interaction, and the influence of the annual cycles are three fundamental factors for understanding the physics of the leading modes (Wang et al. 2008a). Given that in the AMIP-type simulation the atmosphere is purely forced by SST variation, the well-captured part of the first mode should come from the remote El Niño forcing as well as local SST forcing. We have calculated the correlations of seasonal SST anomalies with the PC1. The associated SST anomalies in MME simulation are nearly the same as the observation (figures not shown), confirming the above hypothesis.

Our question here is for the second S-EOF mode. Since the S-EOF2 leads ENSO by 1 yr, it is usually regarded as a precursor for El Niño/La Niña development (Wang et al. 2008a). The success of MME in reproducing the major features of S-EOF2 indicates the dominant role of ocean forcing. Since the second mode exhibits a spectral peak centered at 5 yr, we show the seasonal evolution of associated SST anomalies from JJA(−1) to MAM(1) in Fig. 11. A typical evolution from La Niña to El Niño is evident. Since the only source of AAM rainfall reproducibility in AMIP run comes from the SST forcing, we suggest that the S-EOF2 may be a response to La Niña forcing at decaying stage, although it statistically appears as a precursor for El Niño development. As JJA(0) is the central transitional phase from La Niña to El Niño, the lack of significant anomalous SST forcing leads to a poor skill of MME in capturing the rainfall anomalies. From SON(0) to D(0)JF(1) and MAM(1), the gradually intensified SST anomalies associated with the development of El Niño contribute to the well-captured part of rainfall anomalies associated with S-EOF2.

5. Conclusions

Previous observational analysis has identified two statistically distinguished modes of AAM that represent the highly predictable part of AAM variability. To answer the question whether these leading modes can be captured by AGCM with prescribed SST forcing, 11 AGCMs that participated in the AMIP, which used observational SST to drive AGCMs for the period 1979–99, are evaluated by comparing with the observation. The main findings are listed below.
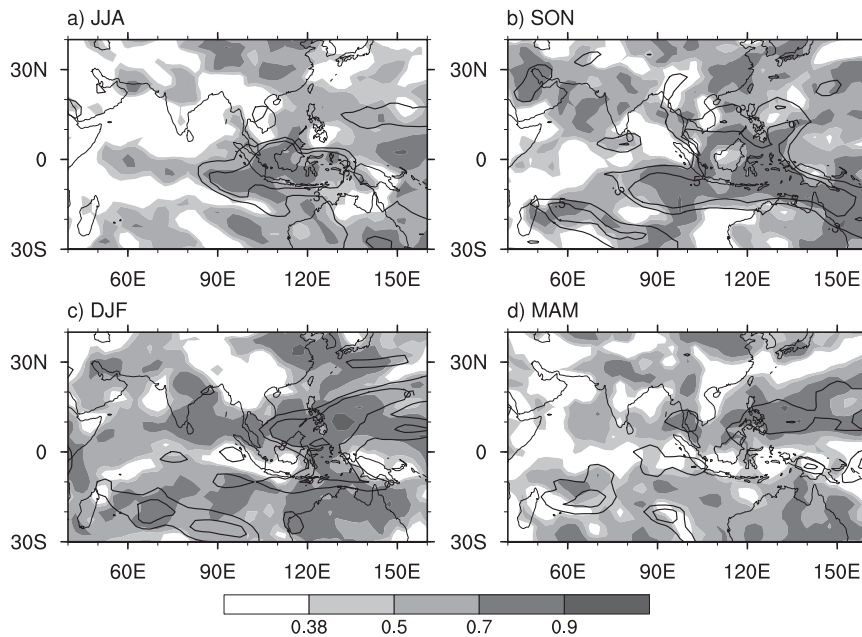
FIG. 10. The spatial pattern of correlation coefficients between the observed and NCEP-2 reanalyzed rainfall anomalies. Only correlations statistically significant at the 10% level are shaded. The percentage variance accounted by the first major mode is shown as contours, which start from 30% with an interval of 20%. (a) JJA, (b) SON, (c) DJF, and (d) MAM.

1) The MME of AMIP simulation captures most part of the realistic features of the spatial structure, seasonal evolution, temporal variations, and the relationship with ENSO in terms of the two major modes of AAM rainfall. The MME reasonably estimates both the biennial tendency and low-frequency of the leading modes. While the first mode generally concurs with the turnabout of El Niño, the second mode is a response to La Niña forcing at decaying stage.

2) The prominent feature of the first leading mode of AAM variability is two seasonal anticyclonic anomalies, the SIO and the WNP ACs. There exists a phase shift in the simulated first dominant mode. The seasonal evolution of both SIO and WNP ACs in AMIP simulation strictly matches that of El Niño remote forcing, while in observation it is not absolutely in phase with ENSO forcing. The reasonable part of AMIP simulation in reproducing the main features of the first leading mode indicates the dominance of remote El Niño forcing in driving interannual variability of AAM, meanwhile the deficiency of AMIP simulation in reproducing the seasonal phase of SIO and WNP ACs suggests the essential role of ocean–atmosphere coupling.

3) The first two leading modes of the interannual variability of AAM mainly reflect rainfall variations over the tropical regions, especially the Maritime Continent, tropical eastern Indian Ocean, and western

Pacific. The MME reasonably captures the two major modes, with results comparable to or even slightly better than those of reanalysis in the tropical regions. Since the two modes explain a high variance of the tropics, the MME presents a high skill in reproducing the total rainfall variability in the region. Over the extratropical western North Pacific and South China Sea, where ocean–atmosphere coupling may be critical for modeling the monsoon rainfall, the MME shows barely any skill, but the reanalysis has higher skill because of the inclusion of part of ocean–atmosphere coupling from the 6–12-h updating cycle.

4) The performance of AMIP simulation in reproducing the leading modes of AAM rainfall is seasonally dependent. The skills of DJF, SON, and MAM are better than that of JJA. This seasonal difference suggests that treating the atmosphere as a response to ocean forcing in DJF and transitional seasons is more reasonable than that in JJA.

5) The MME shows comparable or even slightly better skill than the reanalysis in capturing the tropical signals associated with the two major modes. Although the superiority of MME relative to reanalysis data may stem from the ensemble technique, the GFDL AM2, HadGEM1, and ECHAM5 models are superior to other AGCMs in capturing the leading modes of AAM. Accurate model climatology generally
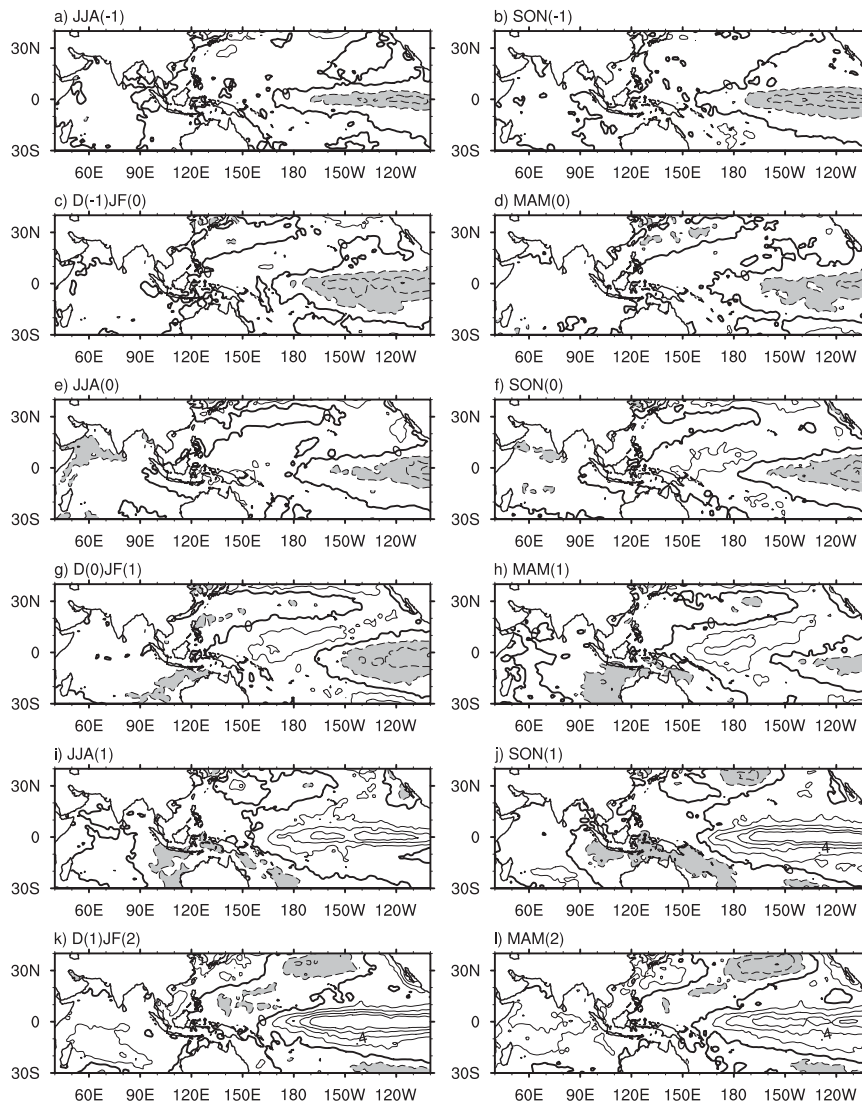
FIG. 11. (a)–(l) Seasonal mean SST anomalies regressed upon the time series of the second S-EOF mode for AMIP MME from JJA(−1) to MAM(2). Solid lines denote positive values, and dashed lines denote negative ones. The contour interval is 0.2°C. Negative values less than −0.1°C are shaded.

coincides with good anomaly patterns associated with the leading modes.

REFERENCES

Hu, Z.-Z., 1997: Interdecadal variability of summer climate over East Asia and its association with 500-hPa height and global sea surface temperature. *J. Geophys. Res.,* **102,** 19 403–19 412.
——, S. Yang, and R. Wu, 2003: Long-term climate variations in China and global warming signals. *J. Geophys. Res.,* **108,** 4614, doi:10.1029/2003JD003651.
Kalnay, E., and Coauthors, 1996: The NCEP/NCAR 40-Year Reanalysis Project. *Bull. Amer. Meteor. Soc.,* **77,** 437–471.
Kanamitsu, M., W. Ebisuzaki, J. Woollen, S.-K. Yang, J. J. Sling, M. Fiorino, and G. L. Potter, 2002: NCEP-DOE AMIP-II Reanalysis (R-2). *Bull. Amer. Meteor. Soc.,* **83,** 1631–1643.
Kang, I.-S., and Coauthors, 2002a: Intercomparison of the climatological variations of Asian summer monsoon precipitation simulated by 10 GCMs. *Climate Dyn.,* **19,** 383–395.

——, and Coauthors, 2002b: Intercomparison of atmospheric GCM simulated anomalies associated with the 1997/98 El Niño. *J. Climate,* **15,** 2791–2805.

Kumar, K. K., M. Hoerling, and B. Rajagopalan, 2005: Advancing Indian monsoon rainfall predictions. *Geophys. Res. Lett.,* **32,** L08704, doi:10.1029/2004GL021979.

Lau, N.-C., and M. J. Nath, 2000: Impact of ENSO on the variability of the Asian–Australian monsoons as simulated in GCM experiments. *J. Climate,* **13,** 4287–4309.

Li, T., Y.-C. Tung, and J.-W. Hwu, 2005: Remote and local SST forcing in shaping Asian–Australian monsoon anomalies. *J. Meteor. Soc. Japan,* **83,** 153–167.

——, P. Liu, X. Fu, B. Wang, and G. A. Meehl, 2006: Spatiotemporal structures and mechanisms of the tropospheric biennial oscillation in the Indo-Pacific warm ocean regions. *J. Climate,* **19,** 3070–3087.

Li, Z.-X., 1999: Ensemble atmospheric GCM simulation of climate interannual variability from 1979 to 1994. *J. Climate,* **12,** 986–1001.

Meehl, G. A., 1987: The annual cycle and interannual variability in the tropical Pacific and Indian Ocean region. *Mon. Wea. Rev.,* **115,** 27–50.

——, and J. Arblaster, 2002: The troposphere biennial oscillation and Asian–Australian monsoon rainfall. *J. Climate,* **15,** 722–744.

North, G. R., T. L. Bell, R. F. Cahalan, and F. J. Moeng, 1982: Sampling errors in the estimation of empirical orthogonal functions. *Mon. Wea. Rev.,* **110,** 699–706.

Rayner, N. A., D. E. Parker, E. B. Horton, C. K. Folland, L. V. Alexander, D. P. Rowell, E. C. Kent, and A. Kaplan, 2003: Global analyses of sea surface temperature, sea ice, and night marine air temperature since the late nineteenth century. *J. Geophys. Res.,* **108,** 4407, doi:10.1029/2002JD002670.

Sperber, K. R., and T. N. Palmer, 1996: Interannual tropical rainfall variability in general circulation model simulations associated with the Atmospheric Model Intercomparison Project. *J. Climate,* **9,** 2727–2750.

Uppala, S. M., and Coauthors, 2005: The ERA-40 Re-Analysis. *Quart. J. Roy. Meteor. Soc.,* **131,** 2961–3012.

Wang, B., Ed., 2006: *The Asian Monsoon.* Springer Praxis, 779 pp.

——, and Q. Zhang, 2002: Pacific–East Asian teleconnection. Part II: How the Philippine Sea anomalous anticyclone is established during El Niño development. *J. Climate.,* **15,** 3252–3265.

——, and S.-I. An, 2005: A method for detecting season-dependent modes of climate variability: S-EOF analysis. *Geophys. Res. Lett.,* **32,** L15710, doi:10.1029/2005GL022709.

——, R. Wu, and X. Fu, 2000: Pacific–East Asian teleconnection: How does ENSO affect East Asian climate? *J. Climate,* **13,** 1517–1536.

——, ——, and T. Li, 2003: Atmosphere–warm ocean interaction and its impact on Asian–Australian Monsoon variation. *J. Climate,* **16,** 1195–1211.

——, I.-S. Kang, and J.-Y. Lee, 2004: Ensemble simulations of Asian–Australian Monsoon variability by 11 AGCMs. *J. Climate,* **17,** 803–818.

——, Q. H. Ding, X. H. Fu, I.-S. Kang, K. Jin, J. Shukla, and F. Doblas-Reyes, 2005: Fundamental challenge in simulation and prediction of summer monsoon rainfall. *Geophys. Res. Lett.,* **32,** L15711, doi:10.1029/2005GL022734.

——, J. Yang, T. J. Zhou, and B. Wang, 2008a: Interdecadal changes in the major modes of Asian–Australian Monsoon variability: Strengthening relationship with ENSO since late 1970s. *J. Climate,* **21,** 1771–1789.

——, and Coauthors, 2008b: How accurately do coupled climate models predict the leading modes of Asian–Australian monsoon interannual variability? *Climate Dyn.,* **30,** 605–619.

Wang, H., 2001: The weakening of Asian monsoon circulation after the end of 1970's. *Adv. Atmos. Sci.,* **18,** 376–386.

Webster, P. J., and S. Yang, 1992: Monsoon and ENSO: Selectively interactive systems. *Quart. J. Roy. Meteor. Soc.,* **118,** 877–926.

Wu, R., and B. Kirtman, 2005: Roles of Indian and Pacific Ocean air–sea coupling in tropical atmospheric variability. *Climate Dyn.,* **25,** 155–170.

Xie, P., and P. A. Arkin, 1997: Global precipitation: A 17-year monthly analysis based on gauge observations, satellite estimates, and numerical model outputs. *Bull. Amer. Meteor. Soc.,* **78,** 2539–2558.

Yang, S., and K. M. Lau, 2006: Interannual variability of the Asian monsoon. *The Asian Monsoon,* B. Wang, Ed., Springer Praxis, 259–293.

Yasunari, T., 1991: The monsoon year—A new concept of the climatic year in the Tropics. *Bull. Amer. Meteor. Soc.,* **72,** 1331–1338.

Yu, R., and T. J. Zhou, 2007: Seasonality and three-dimensional structure of the interdecadal change in East Asian monsoon. *J. Climate,* **20,** 5344–5355.

——, B. Wang, and T. Zhou, 2004: Tropospheric cooling and summer monsoon weakening trend over East Asia. *Geophys. Res. Lett.,* **31,** L22212, doi:10.1029/2004GL021270.

Zhou, T., and R. Yu, 2004: Sea-surface temperature induced variability of the Southern Annular Mode in an atmospheric general circulation model. *Geophys. Res. Lett.,* **31,** L24206, doi:10.1029/2004GL021473.

——, and ——, 2005: Atmospheric water vapor transport associated with typical anomalous summer rainfall patterns in China. *J. Geophys. Res.,* **110,** D08104, doi:10.1029/2004JD005413.

——, and ——, 2006: Twentieth-century surface air temperature over China and the globe simulated by coupled climate models. *J. Climate,* **19,** 5843–5858.

——, ——, H. Li, and B. Wang, 2008a: Ocean forcing to changes in global monsoon precipitation over the recent half century. *J. Climate,* **21,** 3833–3852.

——, L. Zhang, and H. Li, 2008b: Changes in global land monsoon area and total rainfall accumulation over the last half century. *Geophys. Res. Lett.,* **35,** L16707, doi:10.1029/2008GL034881.